Te/CdTe and Al/CdTe Interfacial Energy Band Alignment by Atomistic Modeling

Anthony P. Nicholson,*,† Akash Shah,† Ramesh Pandey,‡ Amit H. Munshi,† James Sites,‡ and Walajabad Sampath†

- † Department of Mechanical Engineering, Colorado State University, Fort Collins, CO 80523, USA
 - ‡ Department of Physics, Colorado State University, Fort Collins, CO 80523, USA

E-mail: apnichol@rams.colostate.edu

Abstract

A synergistic approach that incorporates first-principles atomistic modeling with numerical device simulations is used to systematically evaluate the role of heterointerfaces within metal-chalcogenide-based photovoltaic technologies. Two interfaces involving either a tellurium back contact or aluminum back electrode combined with a cadmium telluride absorber layer within cadmium-telluride-based thin-film solar cells are investigated on an atomic scale to determine the mechanisms contributing to variations in device performance. Electronic structures and predicted charge transport behavior with respect to cadmium and tellurium termination of the absorber layer are studied along the polar oriented CdTe{111} facets. The computational methodology reveals a noticeable contrast between the Schottky barrier forming Al/CdTe interface versus the Type I Te/CdTe heterojunction. Greater band bending features are exhibited by the cadmium termination as opposed to the tellurium termination for each interface case. Subsequent device modeling suggests that 3.6% higher photovoltaic conversion efficiency is achievable for the cadmium termination relative to the tellurium termination of the Te/CdTe

interface. Based strictly on an idealistic representation, both interface models show the importance of atomic-scale interfacial properties for cadmium telluride solar cell device performance with their bulk properties being validated in comparison to published experimental data. The synergistic approach offers a suitable method to analyze solar cell interfaces through a predictive computational framework for the engineering and optimization of metal-chalcogenide-based thin-film photovoltaic technologies.

Keywords

atomistic modeling, photovoltaics, cadmium telluride, tellurium, density functional theory, Green's function, interfaces

1 Introduction

In recent decades, the scientific community has sought to develop a generalized methodology capable of predicting charge transport behavior at interfaces between combinations of material pairs. For metal-chalcogenide-based thin-film photovoltaic (PV) technologies that often comprise of polar bonded semiconductor interfaces, further complexities arise due to the significance of non-stoichiometric effects and distortions of chemical bonds at the interface region. Such challenges make it difficult to obtain a valid description of energy band alignment and accurately observe its impact on device performance, especially for metal-chalcogenide-based PV applications. Conventional theoretical models for band alignment 2,3 within thin-film PV such as Anderson's rule (a.k.a. electron affinity rule) do not account a priori for atomic-scale features resulting from quantum mechanical interactions of polar bonded interfaces. Thus, it is imperative to design a systematic method capable of evaluating the interface-related atomic-scale effects on thin-film PV device performance. In this study, a computational methodology that combines first-principles atomistic modeling with numerical device simulation capabilities is used to probe the limiting factors within metal-

chalcogenide-based interfaces. The proposed methodology is expected to be applicable to various interface problems that are relevant to thin-film PV research communities.

The back contact interface within cadmium telluride (CdTe) thin-film PV is selected as the test region for the proposed synergistic approach. Figure 1 illustrates the typical CdTe-based PV device configuration with the inclusion of either an aluminum (Al) back electrode or tellurium (Te) back contact layer. It is well-known that direct application of a metal back electrode to the CdTe absorber layer forms an excessively large Schottky barrier 1,5,6 that compromises the fill factor of the CdTe PV device. 7,8 An effective solution to decrease the Schottky barrier height has been to introduce a Te layer at the back of the CdTe absorber layer, leading to an improvement in overall open-circuit voltage V_{OC} and fill factor FF for the device. 9,10 It is theorized that an increased hole concentration toward the back of the CdTe layer after adding the Te layer is responsible for the benefits seen in the CdTe-based solar cells. However, the mechanisms for improved charge transport are not clearly understood from an atomic-scale perspective, especially how atomically dependent band alignments at the Te/CdTe interface affect CdTe-based PV device performance as a whole.

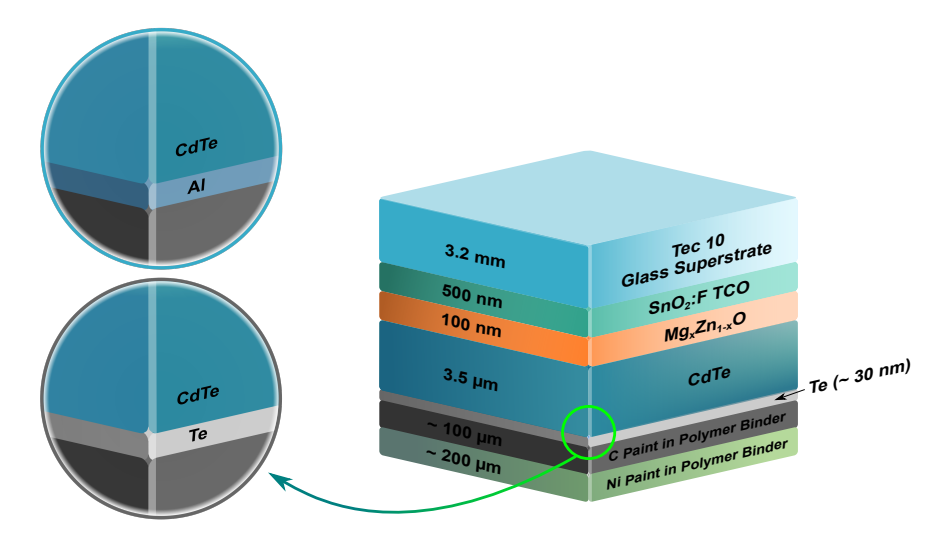


Figure 1: Illustration of typical CdTe PV device configuration with either the Al or Te thin-film layer acting as the back contact.

This study incorporates a synergistic methodology consisting of first-principles modeling and numerical device simulations to investigate the Al/CdTe and Te/CdTe interfaces as

well as their associated mechanisms that impact PV device behaviors. Both the Cd and Te-terminated CdTe facets for each interface are evaluated along the non-stoichiometric low-index CdTe{111} planes to evaluate their differences in electronic structure and potential dipole formations (from hereon, the Cd and Te-terminations of CdTe{111} plane orientations, or CdTe(111) and CdTe(111) planes, will be respectively denoted as t-Cd and t-Te). Outside experimental studies indicate that the CdTe layer has a strong preferred orientation along the {111} plane. The computational results in this study indicate that the relaxed t-Cd Te/CdTe interface case provides the greatest improvement in PV performance due to favorable upward band bending and interface dipole formation that leads to greater effects on the band offsets compared to the relaxed t-Te Te/CdTe interface case. For both interface cases though, the high density of states residing at the Te/CdTe interface may initiate Fermilevel pinning and could explain why the Te back contact is limited in further enhancement of CdTe-based PV devices. The combined workflow between first-principles based atomistic modeling and device modeling offers a predictive way to understand the general role that interfaces play within metal-chalcogenide-based PV technologies.

2 Computational Methods

The following description of the computational work performed in the Al/CdTe and Te/CdTe interface studies consists of the first-principles computations based on density functional theory (DFT) coupled with Green's function (GF) and one-dimensional (1D) numerical device simulations.

2.1 DFT+GF Modeling Framework

All DFT+GF atomistic modeling calculations were performed using the QuantumATK R-2020.09 software package¹² and adopted a linear combination of atomic orbitals (LCAO) basis scheme. The Fritz-Haber-Institute and OpenMX pseudopotentials were respectively

applied to the metallic (Cd, Al) and chalcogenic (Te) species used within each calculation. The DFT+GF models employ the Perdew-Zunger form of the LDA exchange-correlation functional as done in previous CdTe-related computational work. 13,14 An on-site Coulomb interaction parameter in the form of a Hubbard-U correction was applied to the CdTe and Te layers to properly account for orbital contributions that dictate the valence band energy position and maintain each layer's band gap magnitude. U-values of $U_{Cd-4d}=4.6~\mathrm{eV}$ and $U_{Te-5p}=2.55~\mathrm{eV}$ were respectively used on the Cd-4d and Te-5p orbitals within the CdTe layer as done in previous work, 13 resulting in a band gap value comparable to the experimental value of 1.5 eV. 15 For the Te thin-film layer, a U-value of $U_{Te\text{-}5p}=0.73$ eV was applied only to the Te-5p subshell and yielded a Te band gap in good agreement with the experimental value of 0.33 eV. 16 A Monkhorst Pack grid k-point sampling distribution of 7 \times 7 (4.42 Å imes 4.42 Å k-point density in reciprocal space) was used for the transverse directions of the central region of all interface models. Dirichlet boundary conditions were used for both ends of the central region along the transport direction with the left CdTe and right Te (Al) bulk electrodes acting as the semi-infinite regions of each modeling domain. 100 k-points were used for both electrodes in the transport direction to converge their respective electronic structures with the central region ends. A density mesh-cutoff value of 2200 eV was also implemented in all models.

Figure 2 depicts the DFT+GF interface model along with the atomic arrangement of each Te/CdTe and Al/CdTe interface case. The leftmost side of the CdTe layer for each interface model maintained in-plane lattice vector lengths of 4.58 Å with a 60° angle between both vectors. This corresponded to an equivalent representation of the CdTe{111} plane orientation using experimental values and ensured that the calculated electronic properties for CdTe would not be influenced by strain effects from the modified unit cell dimensions after geometry optimization.¹⁷

For the Te/CdTe interface, the entire length of the central region after relaxation was 938.86 Å and 938.51 Å for the t-Cd and t-Te versions, respectively. The Te overlayer was

created using a three-atom primitive semi-infinite cell arranged in a helical manner across the transport direction within a trigonal crystal structure and oriented along the (0001) facet. The construction of the Te/CdTe interface using a lattice-matching method ¹⁸ led to a (1 × 1) in-plane area of the Te layer that was matched to the CdTe unreconstructed surface. Due to the lattice mismatch, the Te layer underwent a mean absolute in-plane strain of 2.03% that resulted in a compressive Poisson strain ($\Delta z/z$, where z is in the transport direction of the Te helical chains) of -1.06% applied to the lengthwise direction of the Te unit cell. The compressive straining effect caused the Te band structure to be slightly modified and thus decreased its band gap value to 0.26 eV.

For the Al/CdTe interface, the relaxed central region lengths were 739.96 Å and 740.03 Å for the respective t-Cd and t-Te cases. The Al layer was oriented such that the (111) plane was in contact with the CdTe{111} planes. The lattice-matching method ¹⁸ forced the cleaved Al surface to adopt a $\sqrt{3} \times \sqrt{3}$ expansion in area compared to its original (111) planar area to match with the CdTe{111} surface. The mean absolute strain on Al was 5.08%, which led to a tensile Poisson strain of +2.69% in the Al layer.

All interfaces underwent a geometry optimization of 10 nm (5 nm on each side of the interface) with a force threshold of 0.01 eV/Å. Electron and hole effective masses from separate DFT bulk calculations for the CdTe and Te layers are reported in Table 1 (see Supporting Information for details of the bulk calculations). The values were found to be in decent agreement with previous computational and experimental literature $^{19-24}$ after the implementation of the Hubbard-U correction. The effective masses were used for quantifying certain parameters within the numerical device simulations found in the proceeding section.

Table 1: Electron and hole effective masses for the CdTe{111} and Te(0001) layers.

Layer	m_n^*	m_p^*
CdTe{111}	0.13	1.25
Te(0001)	0.06	0.17

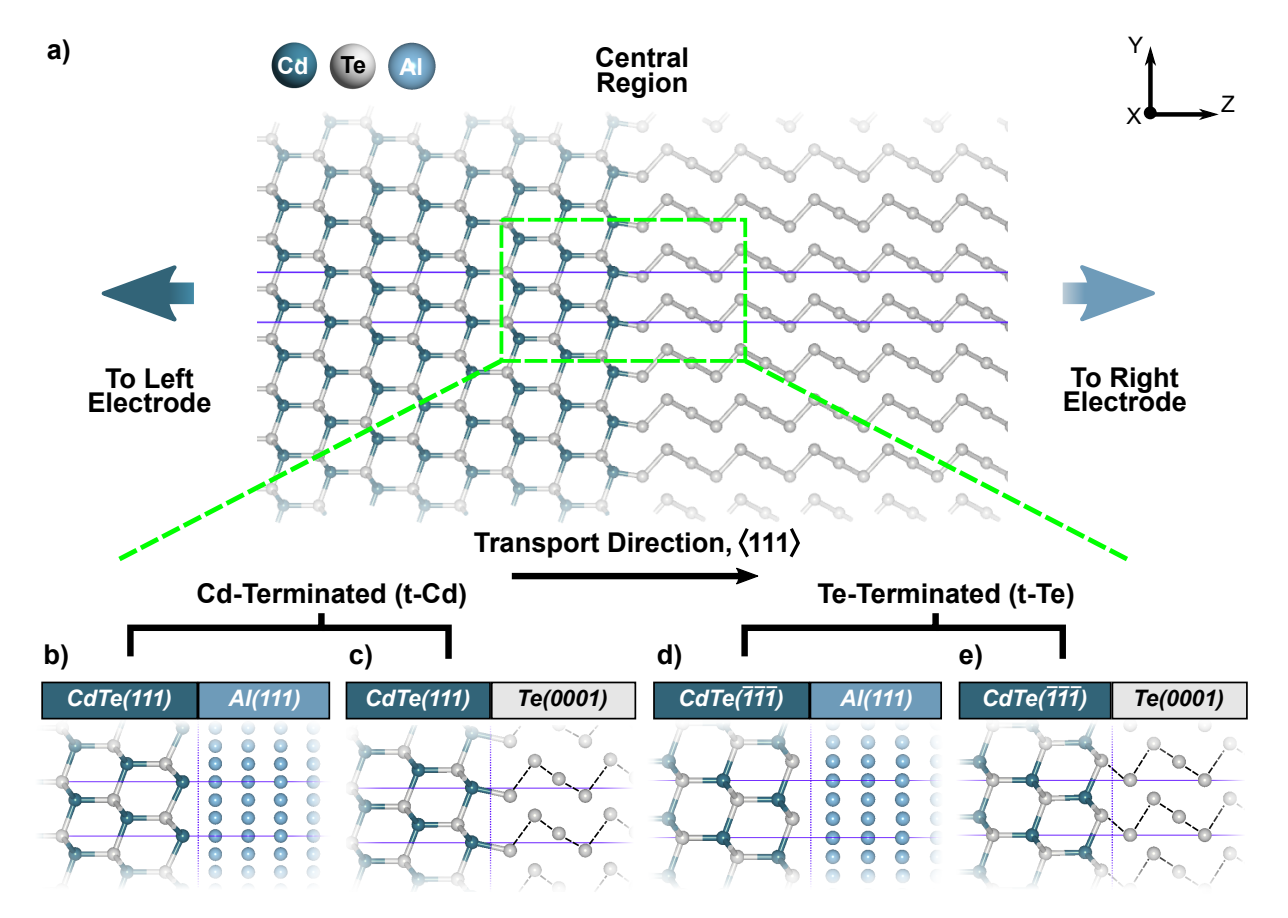


Figure 2: (a) DFT+GF Te/CdTe interface model made up of two semi-infinite bulk electrodes and a central region. The purple lines mark the regions of periodicity for the supercell configuration. The green dashed rectangle is zoomed in as shown in (b)-(e) for clarity of the interface type, either t-Cd or t-Te versions of the Al/CdTe and Te/CdTe interfaces, respectively. For each interface, the vertical purple dashed line is positioned where the two layers meet to form the interface. The dotted lines connecting the Te atoms in c) and e) are included to simply show the bonding arrangement leading to the helical chain structure for the Te thin-film layer.

2.2 Numerical Device Modeling Setup

Prior to simulating the CdTe PV device performance, several parameters were extracted from all DFT+GF interface models and integrated with numerical device simulations. The SCAPS-1D device simulation software ²⁵ was utilized to assess the impact of variations within the Te/CdTe and Al/CdTe interfaces on PV device performance. The key parameters of the SCAPS-1D setup is found in Table 2 for the CdTe-based PV device arrangement (Figure 1). Appropriate modeling parameters that were not obtained using the DFT+GF method

were collected from published device simulation-based literature $^{26-29}$ and used in the current work. A series and shunt resistance of $1~\Omega\cdot\text{cm}^{-2}$ and $10^3~\Omega\cdot\text{cm}^{-2}$, respectively, were used since they are typical of CdTe-based solar cells. Measured bulk lifetimes of CdTe without selenium alloying tend to remain on the lower end of the range between 1 to 100 ns. 30,31 For the device models performed in this study, the CdTe layer maintained a uniform hole bulk lifetime of ~ 10 ns and electron bulk lifetime ranging between 3 to 10 ns (depending on the location being the bulk or interface region for CdTe). No bulk absorber defect energies were incorporated in the SCAPS-1D models to strictly focus on how interfacial effects contribute to the CdTe PV device performance. A nonohmic back contact barrier magnitude of 0.3 eV was used for only the Te/CdTe SCAPS-1D simulations.

The effective density of states within the conduction and valence bands was quantified using the effective mass $m_{n/p}^*$ calculated via DFT with the following expression:

$$N_{C/V} = 2\left(\frac{2\pi m_{n/p}^* kT}{h^2}\right)^{3/2} \tag{1}$$

where k is Boltzmann's constant, T is temperature, and h is Planck's constant. Furthermore, the thermal velocity for the charge carriers can also be determined from the effective mass:

$$\nu_{n/p} = \sqrt{\frac{3kT}{m_{n/p}^*}} \tag{2}$$

The SCAPS simulation results were found to be minorly sensitive to the quantified parameters using the effective mass calculated in this study compared to parameters used in past studies. ²⁶ The open circuit voltage and fill factor decreased using the parameters found in Table 2 by an average of 9 mV and 0.4%, respectively, thereby causing the power conversion efficiency to change by only around 0.3%.

Table 2: SCAPS-1D device modeling parameters for the CdTe-based PV device*.

Parameters	F:SnO ₂	MgZnO	p-CdTe _{bulk}	$p\text{-}CdTe_{int}$	p ⁺ -Te
Thickness, $L \text{ (nm)}$	500	100	2940	60	30
Band Gap, E_g (eV)	3.60	3.50	1.50	†	0.26
Electron Affinity, χ (eV)	4.00	4.00	4.13	†	4.59
Relative Permittivity (ϵ/ϵ_0)	9.0	10.0	9.4	10.0	28.0
$_{N_{C}~(\mathrm{cm}^{ ext{-}3})}^{ ext{DOS},}$	2.2×10^{18}	1.1×10^{18}	1.1×10^{18}	1.1×10^{18}	3.8×10^{17}
$_{N_{V}~(\mathrm{cm}^{ ext{-}3})}^{ ext{DOS},}$	1.8×10^{19}	1.8×10^{19}	3.5×10^{19}	3.5×10^{19}	1.8×10^{18}
Thermal Velocity, $\nu_n \text{ (cm/s)}$	1.0×10^7	1.0×10^7	3.3×10^7	3.3×10^7	4.7×10^7
Thermal Velocity, $\nu_p \; ({\rm cm/s})$	1.0×10^7	1.0×10^7	1.0×10^7	1.0×10^7	2.8×10^7
Doping Density, $n \text{ (cm}^{-3})$	1×10^{18}	2×10^{14}	N/A	N/A	N/A
Doping Density, $p \text{ (cm}^{-3})$	N/A	N/A	5×10^{13}	5×10^{13}	7×10^{19}
Electron Mobility, $\mu_n \text{ (cm}^2/\text{V·s)}$	100	100	320	320	50
Hole Mobility, $\mu_p \; (\text{cm}^2/\text{V·s})$	25	25	40	40	175
Electron Lifetime, τ_n (ns)	-	-	3	10	-
Hole Lifetime, $\tau_h \text{ (ns)}$	-	-	10	10	-

 $^{^{*}}$ The Te/CdTe SCAPS-1D models include a 0.3 eV back barrier based on experimental results.

 $^{^\}dagger$ Imported as spatial-dependent tabular data into device simulation parameter entry

One important remark must be made prior to the integration of the DFT+GF results with the SCAPS-1D device simulations. Since the DFT+GF models only focus on a pristine defect-free interface made up of two single-crystal bulk materials, the intrinsic Fermi level position for CdTe and Te are too high to be classified as respective p and p⁺-type layers as assumed for the SCAPS-1D models. The CdTe layer is often described as intrinsically p-type due to the presence of native point defects such as Cd vacancies within CdTe thinfilms deposited or grown through various techniques. 32-34 Similarly, the p-type nature of Te thin-films can be attributed to crystallographic defects leading to additional acceptor centers within the film itself.³⁵ However, the computed effective masses for single-crystal CdTe and Te cause the intrinsic Fermi levels to sit much closer to the midgap energy of each bulk material's bandgap than the valence band to maintain charge neutrality (please see Supporting Information for the calculation). As a result, the CdTe and Te layers will not exhibit the desired lower Fermi level position unless higher p-type doping concentrations are somehow applied to each layer. Within QuantumATK, an atomic compensation charge was used to adjust the ion charge of the atoms in the CdTe and Te regions, thus influencing each region's electrostatic potential and thus Fermi level position with respect to the potential to simulate the p-type doping effect. In this study, it was determined that an atomic compensation charge of 7×10^{19} cm⁻³ was sufficient within the Te layer to simply move the Fermi level downward as expected but not affect the calculated energy band alignment features. As for the CdTe layer, the atomic compensation charge magnitude of 2×10^{14} cm⁻³ was used but there was negligible effect on the Fermi level position due to its smaller magnitude compared to the Te atomic compensation charge. By including the atomic compensation charges, it was assumed that quantitative band alignments could be directly translated to the SCAPS-1D models.

3 Results & Discussion

3.1 Energy Band Alignment

The projected local density of states (PLDOS) calculated by the DFT+GF method for each Al/CdTe and Te/CdTe interface is presented in Figure 3 as a description of the interfacial band alignments. Pertinent features were measured for each PLDOS plot to quantify their energy magnitudes and use them within the SCAPS-1D device simulations. Table 3 lists the magnitudes of each measured feature obtained from the macroscopically averaged valence and conduction band edges traced within each interface model. The bulk band gap values for the CdTe and Te layers are well-converged for long screening lengths accommodated by larger supercells coupled to semi-infinite regions for each model. The DFT+GF method is a strong alternative to traditional periodic slab models ^{36,37} for obtaining energy band gaps, offsets, and alignment levels for various interfaces. The valence (conduction) band offset $\Delta E_V (\Delta E_C)$ is defined as the energetic distance between points 1 and 2 (points 3 and 4) along the valence (conduction) band edge of the Te/CdTe interfaces as shown in Figures 3b and 3d. The CdTe side of the models have band gap magnitudes that are in good agreement with the experimental value of 1.5 eV. 15,38 The Te band gap tends to be smaller than the expected value of 0.33 eV^{16,39} due to additional lattice-mismatch strain that leads to the formation of a deformation potential as outlined in other work. 40-42

In general, the Al/CdTe interface models form a Schottky barrier along with metal-induced gap states (MIGS) that extend approximately 10 Å within the CdTe layer. On the other hand, the Te/CdTe interfaces correctly predict a Type I heterojunction with electronic states residing within the Te overlayer nearest the interface region. The valence band offsets of both Te/CdTe interface models ($\Delta E_V = 0.41$ eV, 0.75 eV) are in agreement with values ranging between 0.5-0.6±0.1 eV as determined via photoelectron spectroscopic characterization techniques. ⁴³⁻⁴⁵

There are subtle differences when comparing the t-Cd and t-Te versions of the Al/CdTe

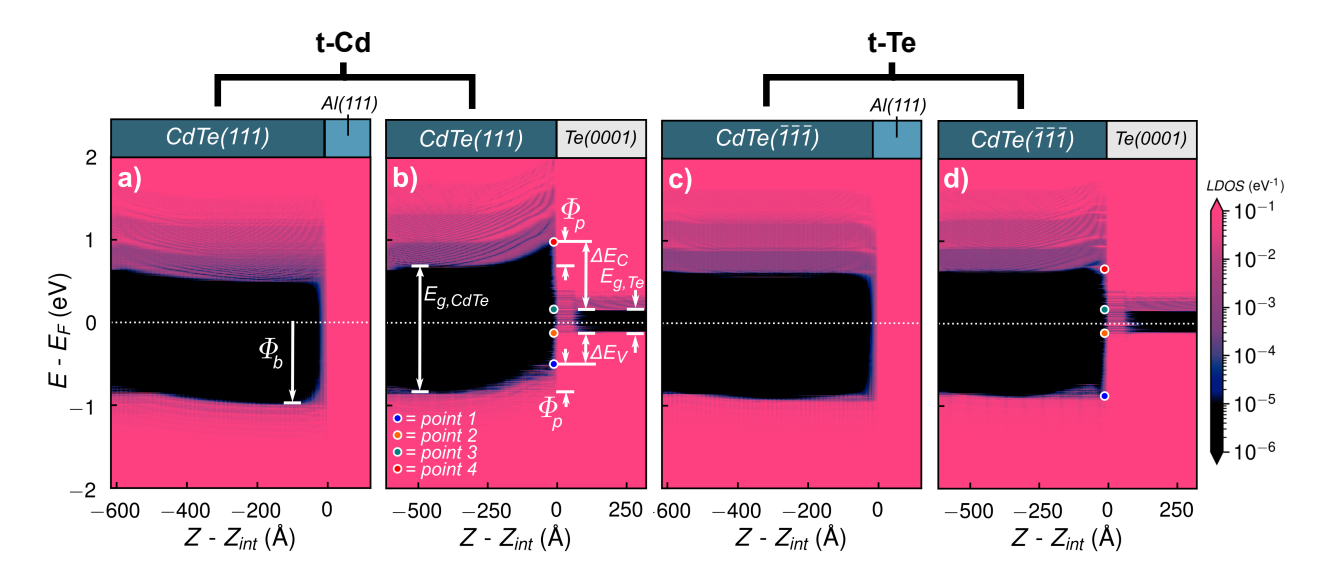


Figure 3: PLDOS plots depicting the energy band alignments of the t-Cd (a, b) and t-Te (c, d) versions of the Al/CdTe and Te/CdTe DFT+GF interface models, respectively. The x-axis is referenced from the interface position Z_{int} (reported in Table 3) of each model. Example labels for all pertinent band alignment features recorded in Table 3 are provided in (a) and (b) as visual references. The colored point labels in (b) indicate where the valence and conduction band offsets are measured for the Te/CdTe interface models. The PLDOS plots shown for the Te/CdTe interfaces have an atomic p-type compensation charge applied to the Te layer with a magnitude of 7×10^{19} cm⁻³. The pink regions indicate high density of states while black regions represent negligible density of states. The zero energy on the y-axis is referenced by the Fermi level E_F (dotted line) of each respective band alignment profile.

interfaces in relation to band bending and Schottky barrier height. The t-Cd case (Figure 3a) shows a slight downward band bending effect that tends to increase the Schottky barrier height by 0.06 eV in comparison to the flatter band alignment of the t-Te case (Figure 3c). The Schottky barrier magnitudes Φ_b found in this work (0.98 and 0.92 eV for the respective t-Cd and t-Te cases) are larger than previous DFT calculations performed by *Odhkuu et al.* (i.e., $\Phi_b = 0.55 - 0.82$ eV). ⁴⁶ However, they used a tellurium-metal-alloy configuration as the adlayer while this work simply considers Al(111) in direct contact with the CdTe termination layer. If all band alignment features were retained with higher p-type doping in CdTe, the Schottky barrier would decrease in response. Figure 4a provides a schematic representation of the band diagram across the entire PV device under illumination and in forward bias at V = 0.6 V using the SCAPS-1D parameters specified in Table 2. The conceptualized

Table 3: Calculated electronic features obtained from the PLDOS plots in Figure 3 for the t-Cd and t-Te versions of the Al/CdTe and Te/CdTe DFT+GF interface models, respectively. All measured energy values are within ± 0.01 eV.

Interface	Z_{int} (Å)	$E_{g,CdTe}$ (eV)	$E_{g,Te}$ (eV)	$\Delta E_C \text{ (eV)}$	$\Delta E_V (\text{eV})$	$\Phi_b \; (\mathrm{eV})$	$\Phi_p \text{ (eV)}$
(t-Cd) Al/CdTe	617.52	1.45	N/A	N/A	N/A	-0.98	N/A
$\begin{array}{c} \text{(t-Cd)} \\ \text{Te/CdTe} \end{array}$	617.62	1.47	0.25	0.77	0.41	N/A	+0.26
$\frac{\text{(t-Te)}}{\text{Al/CdTe}}$	617.38	1.46	N/A	N/A	N/A	-0.92	N/A
m (t-Te) $ m Te/CdTe$	617.40	1.48	0.44	0.70	0.75	N/A	+0.04

charge transport behaviors at the Cd and Te-termination of the Al/CdTe interfaces (Figure 4b and 4d) show that the majority hole carriers would be strongly reflected from the back and significantly impact the V_{OC} of the PV device. In addition, the presence of MIGS in both cases would lead to high recombination velocities at the back as typically seen for metal electrodes directly contacted to the CdTe layer.

The Te/CdTe interface cases demonstrate more pronounced features than the Al/CdTe band alignment profiles. For both the t-Cd and t-Te cases (Figure 3b and 3d), there is noticeable upward band bending that creates a visual cusp-like feature in both the valence and conduction bands. The band-edge discontinuity for the t-Cd case, however, exhibits greater band bending with a large potential height Φ_p of +0.26 eV above the valence band maximum and conduction band minimum of the bulk-like CdTe region. On the other hand, the t-Te case exhibits a smaller magnitude at +0.04 eV. The cusp-like feature has been evaluated in previous DFT+GF surface calculations for CdTe^{13,47} and is partly attributed to the applied localized strain on the atomic positions caused by geometry optimization. The band bending potential Φ_p was verified to exist regardless of whether atomic relaxation was applied or not to the Te/CdTe interface. Both long-range (100-200 Å) space charging and short-range (<10 Å) interfacial dipole effects contribute to the band alignment characteristics

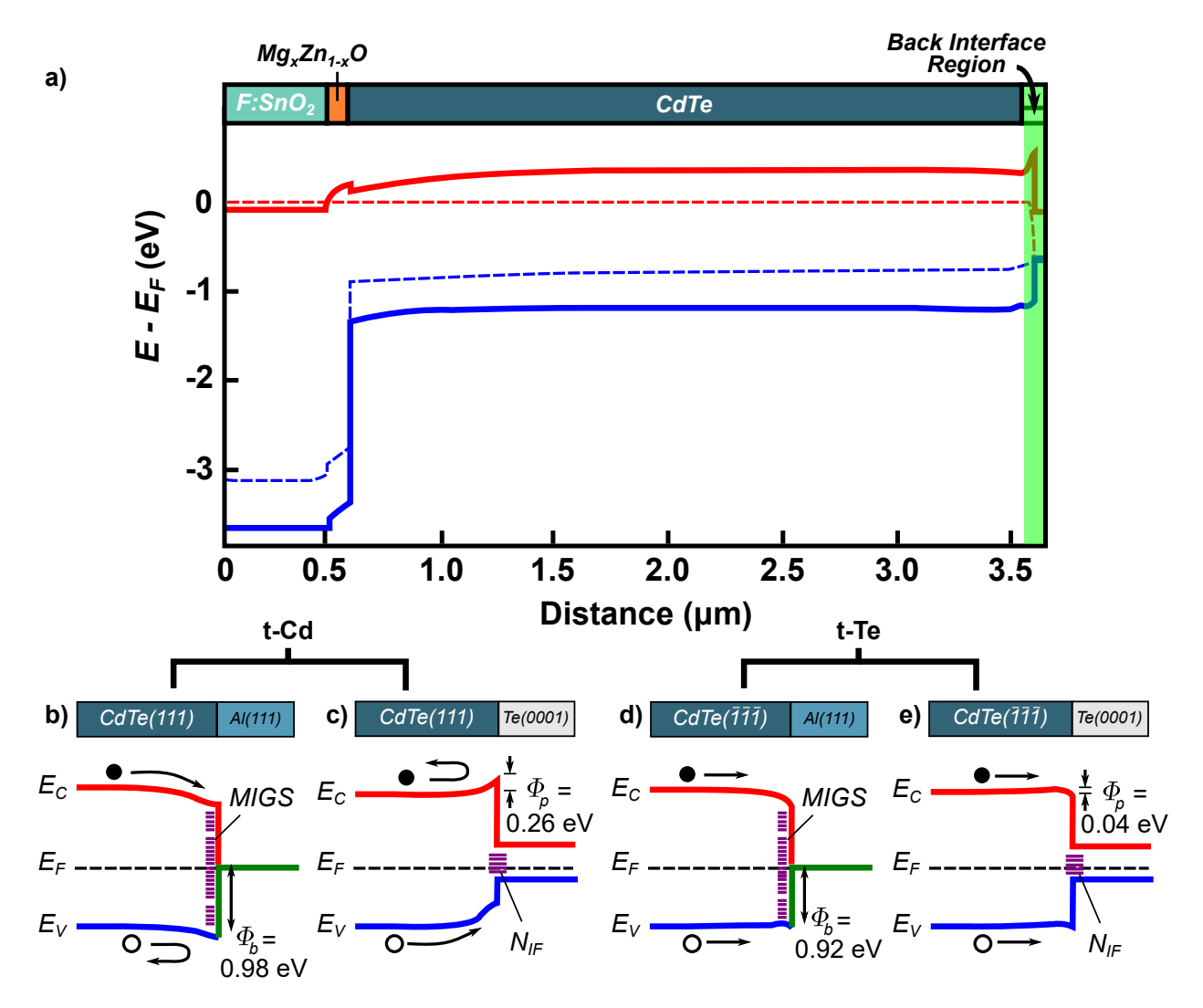


Figure 4: a) Schematic representation of the band alignment for the simulated CdTe-based PV device configuration under illumination and at a forward bias of 0.6 V. The red and blue solid lines respectively denote the conduction and valence bands while the red and blue dotted lines are the electron and hole quasi-Fermi levels. The back interface region of interest in the current work is highlighted in green for the conceptualized band alignments of the Al/CdTe and Te/CdTe interfaces. b) thru e) depict the expected charge transport behaviors based on the calculated energy band alignments in Figure 3 for the t-Cd (b, c) and t-Te (d, e) versions of the Al/CdTe and Te/CdTe interfaces, respectively. Electrons are labeled as black circles while the holes are labeled as open circles. "MIGS" indicate the presence of metal-induced gap states for the Al/CdTe interface while " N_{IF} " specify the interface states residing within the Te layer of the Te/CdTe interface. Note that the Fermi level E_F is shifted downward to indicate that the CdTe and Te layers are respectively p and p⁺-type layers as modeled in the SCAPS-1D simulations.

present at the Te/CdTe interface. Fritsche et al. state that the Te layer serves to establish a tunneling effect and conclude that the Te back contact does not create an Ohmic contact between CdTe and the metal electrode. They specify that a p⁺-doping mechanism at the back of CdTe leads to favorable band alignment conditions. The current work offers another possible explanation by demonstrating that the localized strain, induced long-range space charges, and the interfacial dipole residing at the polar Te/CdTe interface achieve a similar band alignment profile. Under the present conditions, Φ_p is clearly larger for the Cd-termination than the Te-termination. As a result, the t-Cd version of the Te/CdTe interface should conceptually provide better charge carrier selection toward the back of the CdTe-based PV device (Figure 4c) as opposed to the t-Te case (Figure 4e). This idea is further supported by the device simulations performed in the current study. The complex interfacial band alignment features due to relaxation effects and termination layers reveal the importance of using first-principles calculations to account for microscopic details that empirical band alignment models such as Anderson's rule cannot address. The same services are stables as a state of the same services are stables as a state of the same services and termination layers reveal the importance of using first-principles calculations to account for microscopic details that empirical band alignment models such as Anderson's rule cannot address.

Another highlightable characteristic is the region of electronic states that reside within the Te gap. Dangling bond formation is responsible for the high density of electronic states and is expected to influence the Fermi level position. The electronic states reach nearly 80 Å within the Te layer with their spatial extension likely due to the atomic relaxation within the vicinity of the Te/CdTe interface region. A similar change in electronic structure of the Te overlayer for thicknesses less than 25 Å was observed in XPS measurements of binding energy and was concluded to be due to the amorphous nature of the Te layer at lower coverage. Another experimental study reported that there is a transition from n-type to p-type behavior for thicknesses greater than 76 Å for an evaporated Te layer. Multiple factors may be responsible for the phenomena seen within the two studies. However, the current work does offer one explanation by showing that the Te layer creates a large DOS that extends as a function of the amount of atomic relaxation applied to the interface region. As a result, the Te/CdTe interface model suggests that the Te electronic band structure is quite sensitive

to the strain induced by the initial lattice mismatch and subsequent atomic relaxation, both of which tend to modify the metalloid Te layer to behave more like a metal in these localized regions. A strong pinning effect was observed despite varying the Te p-type compensation charge from 10¹⁸ to 10²⁰ cm⁻³ within the interface model (see Supporting Information for further details). These electronic states are expected to increase recombination at the interface and counteract the beneficial aspects of upward band bending and enhanced hole transport for the Te/CdTe interface. In consequence, the extraneous electronic states in the Te overlayer could potentially act as a charge transport bottleneck that limits the beneficial aspects of the Te back contact within CdTe-based PV.

3.2 Interfacial Dipole Formation

In an effort to further distinguish among the Al/CdTe and Te/CdTe interface configurations, an evaluation of interfacial dipole formation was performed with respect to termination layer. The induced electron density displacement $\Delta \rho_{ind}(z)^{50}$ for each interface model is a combination of the interfacial effects (i.e. relaxation, termination layer, etc.) contributing to the interfacial dipole and is calculated using the following equation:

$$\Delta \rho_{ind}(z) = \rho_{B/A}(z) - (\rho_B(z) + \rho_A(z)) \tag{3}$$

In Equation 3, $\rho_{B/A}(z)$ is the in-plane averaged electron density of the DFT+GF model for either the Al/CdTe or Te/CdTe interface while $\rho_B(z)$ and $\rho_A(z)$ are the isolated in-plane averaged electron densities for each bulk material (i.e., A = CdTe, B = Al, Te) using their equivalent DFT+GF surface models (see Supporting Information for further details). The calculated induced interfacial dipole μ_{ind}^{int} after integrating the induced electron density displacement across a 20 Å range within the interface region is calculated as:

$$\mu_{ind}^{int} = -e \int^{int} z \cdot \Delta \rho_{ind}(z) dz \tag{4}$$

The magnitude for the induced interfacial dipole is expressed in Debye per unit area $(D \cdot Å^{-2})$. A negative sign for μ_{ind}^{int} indicates that the dipole points from the B layer toward the A layer and vice versa for a positive sign. The potential (energy) step due to the interface dipole can then be defined as:

$$\Delta = \frac{e \cdot \mu_{ind}^{int}}{\varepsilon_0} \tag{5}$$

Figure 5 depicts the interfacial dipole formation across both the Al/CdTe and Te/CdTe interfaces while Table 4 quantifies the magnitude and direction of the induced dipole as well as potential step. The potential step Δ indicates the level of contribution that the interfacial dipole has on the band alignment found for each respective interface. ⁵¹ As indicated in Table 4 for the Te/CdTe interfaces, the Cd-termination shows a larger potential step value (0.32 eV) than the Te-termination (0.08 eV). As a result, the interface dipole leads to a larger effect on the valence and conduction band-edge discontinuities for the t-Cd Te/CdTe interface.

There are notable differences between the t-Cd and t-Te cases for both interfaces. For the Cd-terminations, the dipole points toward the left and indicates that the negative charging occurs on the overlayer side to assist in the large band alignment shifts at the interface. On the other hand, the Te-terminations have a positive value for μ_{ind}^{int} and thus have dipoles pointing from the CdTe side to the Te side of the interface (toward the right). The calculated effects of interfacial dipoles on the Al/CdTe and Te/CdTe interfaces reveal that short-range charge rearrangement plays a larger role than expected for the t-Cd cases and may suggest the cationic termination layer to be more favorable for band alignment and charge transport.

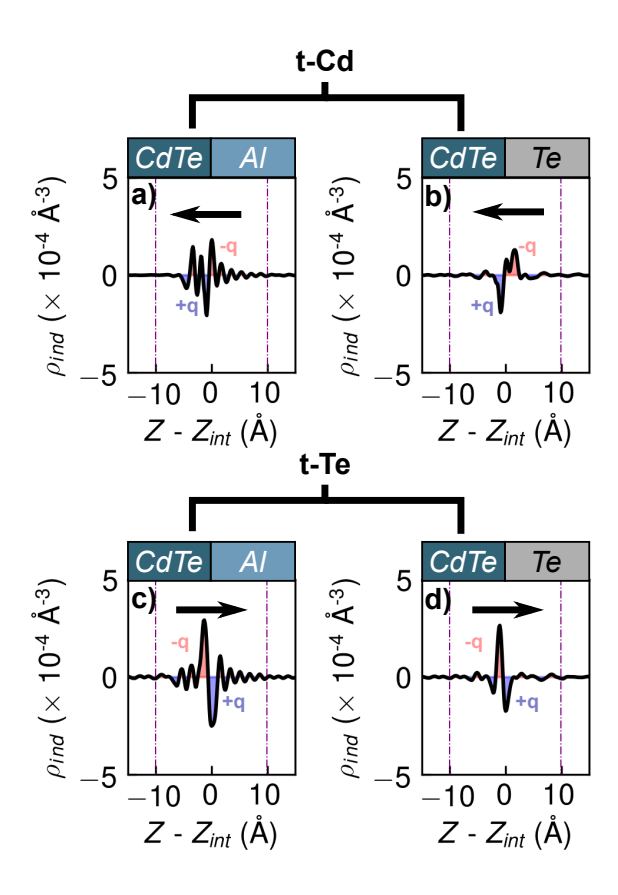


Figure 5: Interfacial dipole plots of the t-Cd (a, b) and t-Te (c, d) versions of the Al/CdTe and Te/CdTe DFT+GF interface models, respectively. The red and blue shaded regions indicate charge accumulation and depletion at the interface region. The purple dashed lines mark the limits of integration for the induced interfacial dipole μ_{ind}^{int} calculation in Equation 4. The arrows indicate the net dipole direction going from negative charging to positive charging for each interface region.

3.3 Device Simulations

The integration of first-principles computational modeling with SCAPS-1D device simulations provides a unique perspective into the CdTe-based PV device performance with respect to the selected back contact interface. The relevant description of energy band alignment between the CdTe absorber layer and the back contact layers (Al or Te) for device modeling tasks enables a thorough discussion on the effect of the termination layer on PV charge transport behaviors along the highly polar {111} facets. For the Te/CdTe interface-based device simulations, a uniform distribution of total interfacial defect density ($N_{IF,tot}$: 1 × 10¹¹ cm⁻²) accompanied by total defect states ($N_{t,tot}$: 1 × 10¹⁷ cm⁻³) were respectively applied to

Table 4: Interfacial dipole formation and potential (energy) step across the Cd and Teterminations of the Al/CdTe and Te/CdTe interface models, respectively. The Te layer has an atomic p-type "compensation" charge of 7×10^{19} cm⁻³.

Interface	Dipole, μ_{ind}^{int} (D·Å ⁻² × 10 ⁻³)	Potential Step, Δ (eV)	Direction
(t-Cd) Al/CdTe (t-Cd) Te/CdTe	-1.01 -1.76	-0.18 -0.32	← ←
(t-Te) Al/CdTe (t-Te) Te/CdTe	$+1.61 \\ +0.46$	$+0.29 \\ +0.08$	$\begin{array}{c} \rightarrow \\ \rightarrow \\ \rightarrow \end{array}$

the Te/CdTe interface and 80 Å of the Te layer to qualitatively represent their presence as shown in the band alignment plots.

Figure 6 provides the SCAPS-1D simulated JV curves for each interface model. Relevant measurements such as open-circuit voltage (V_{OC}), short-circuit current (J_{SC}), fill factor (FF), and power conversion efficiency (PCE) are recorded in Table 5. For each SCAPS-1D device simulation, the CdTe layer maintained an absorber doping concentration magnitude of 5 × 10^{13} cm⁻³ to depict a solar cell with no intentional doping. The Te back contact doping concentration was maintained at 7 × 10^{19} cm⁻³ to set the Fermi level position such that the Te layer would be classified as p⁺-type (note that typical p-type concentrations reported for evaporated Te thin-film layers reside between $\sim 10^{18}$ to 10^{19} cm^{-3 35,52}). All other parameters remained unchanged for each device simulation.

As expected, the Al/CdTe device simulations show a much lower *PCE* than the Te/CdTe-based simulations due to the large Schottky barrier formation that mitigates the majority hole charge transport toward the back of the PV device. In Figure 6, the Cd-termination of the Al/CdTe interface results in a slightly lower open-circuit voltage than the Te-termination. This is likely due to the additional downward band bending and thus a marginal increase in Schottky barrier magnitude than the t-Te case, leading to a 0.2% *PCE* decrease. The simulated results confirm the importance of reducing or eliminating the Schottky barrier that is often responsible for the fill factor and open-circuit voltage losses at the back interface of

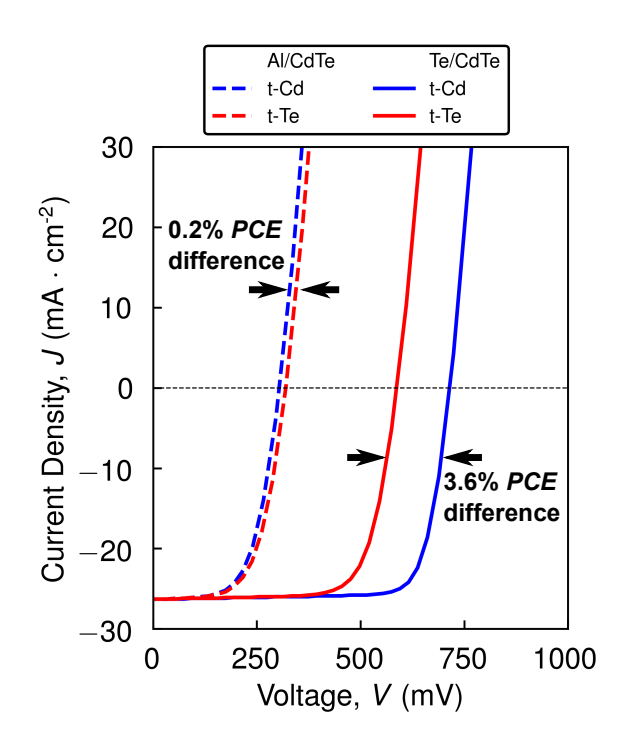


Figure 6: Simulated JV data for the CdTe-based PV device shown in Figure 1 for the t-Cd and t-Te versions of the Al/CdTe and Te/CdTe interfaces.

CdTe-based PV technologies.

The resulting JV parameters as shown in Table 5 clearly demonstrate how termination layer may play a larger role on the predicted device performance than expected for the CdTe PV device. For the Te/CdTe interface, there is an increase in PCE of 3.6% solely due to the band alignment differences between the Te-termination to Cd-termination. The t-Cd Te/CdTe interfacial band alignment impedes minority charge carriers from moving toward the back while enhancing the flow of majority charge carriers due to its smaller valence band offset. The Te-termination, on the other hand, displays a smaller dipole effect in the band edge and larger valence band offset that results in a lower FF and V_{OC} . The inherent upward band bending and more favorable band-edge discontinuities for the Cd-termination emphasize the importance of terminating species and charge rearrangement at the back interface for better overall PV performance. As for the interfacial defect densities, there are minimal changes to the overall device performance. There is no immediate connection

Table 5: Measured JV data for the SCAPS-1D simulations of the CdTe-based PV device containing either the Al/CdTe or Te/CdTe back interface models. For the Te/CdTe simulations, the uniformly distributed total interfacial defect density $N_{IF,tot}$ and trap defect states $N_{t,tot}$ are specified as 1×10^{11} cm⁻² and 1×10^{17} cm⁻³, respectively.

Interface	$V_{OC} (\mathrm{mV})$	$J_{SC} (\mathrm{mA \cdot cm^2})$	FF (%)	<i>PCE</i> (%)
(t-Cd) Al/CdTe	305	26.3	61.5	4.9
(t-Te) Al/CdTe	320	26.3	61.1	5.1
(t-Cd) Te/CdTe	716	26.3	78.9	14.9
(t-Te) Te/CdTe	588	26.3	73.3	11.3

to explaining the importance of interfacial defect densities on Fermi-level pinning for the Te/CdTe interface with the current study. Fermi-level pinning is likely to exist for the Te/CdTe interface and in general is known to decrease overall PV device performance.

According to the results obtained by the SCAPS-1D device simulations integrated with the DFT+GF method, the cationic termination of the CdTe layer along the {111} planar family is expected to increase the efficiency of CdTe-based PV devices. However, limitations on the controllability of termination within both single crystal and polycrystalline CdTe thinfilm layers create several experimental challenges to achieving a higher PCE. In CdTe single crystal cases, surface reconstructions are known to be more energetically favorable for polar bonded surfaces like the {111} planes⁵³ unless careful preparation in annealing and species flux conditions are used during CdTe deposition. ⁵⁴ In turn, it is expected that energy band alignment would change in response to surface reconstruction since previous DFT work on reconstructed CdTe surfaces indicate flatter, well-behaved valence and conduction band edges in comparison to the unreconstructed cases. ^{13,14} Furthermore, the Fermi-level pinning due to the high density of Te/CdTe interface defect states requires a higher Te doping to overcome it. Carrier concentration within the p^+ -Te layer tends to reside within the high 10^{18} to low 10¹⁹ range and thus poses an additional obstacle if higher Te doping (as was implemented in the current study) was desirable for greater performance. Nonetheless, the computational approach utilized for both the Al/CdTe and Te/CdTe interfaces indicates how differences in termination layer and elemental species modify band alignment and defect characteristics that can potentially be controlled to optimize the performance of CdTe-based PV devices.

4 Conclusion

The synergistic computational methodology consisting of first-principles and 1D numerical device calculations was performed in this study using the Al/CdTe and Te/CdTe interfaces as test cases. The energy band alignment details and device simulation results provide several key insights that conventional band alignment models such as Anderson's rule do not address. Firstly, the Schottky barrier formation as well as valence and conduction band offsets calculated using atomistic modeling are closely supported by experimental evidence from past literature for the Al/CdTe and Te/CdTe interfaces. Secondly, the DFT+GF method provides a detailed description of both the electronic structure and band alignment features such as the combined band bending potential and interfacial dipole effects along with interface states that encourage Fermi-level pinning. Lastly, there is a notable contrast between the t-Cd and t-Te versions of the Al/CdTe and Te/CdTe interface as portrayed by the device simulations. For the Te/CdTe interface, the t-Cd case leads to more pronounced upward band bending and thus enhanced carrier selection at the back of the CdTe-based PV device leading to improved V_{OC} and FF.

The Al/CdTe and Te/CdTe DFT+GF interface models demonstrate the effectiveness of computational modeling for studying how morphological factors associated with the interface region significantly modify the electronic features present at the interface. At the same time, the integration of first-principles derived material properties with the device simulation tools depict the efficacy of combining atomistic modeling with physical device modeling efforts to accurately predict PV device performance. The data-driven predictions of interface-related phenomena obtained within the current study offers a synergistic computational methodology that could later prove useful for the metal-chalcogenide-based thin-film PV industry.

Supporting Information

Additional details of DFT bulk parameters, effect of atomic compensation charges on intrinsic Fermi level, and interface dipole comparison between slab and surface Green's function methods

Acknowledgements

The authors thank Stephan Lany, Petr Khomyakov, and Umberto Martinez for their thoughtful discussions and critique of the current research work. Anthony P. Nicholson received funding from the National Science Foundation MPS-Ascend Postdoctoral Research Fellowship under Grant No. 2138081. Anthony P. Nicholson, Akash Shah, and Walajabad Sampath received funding from the National Science Foundation under the Industry/University Cooperative Research Center (I/UCRC) for Next Generation Photovoltaics program and the I/UCRC for Next Generation Photovoltaics Industrial Advisory Board (Award No. 1821526 and 2052735). Any opinions, findings, and conclusions or recommendations expressed in this material are those of the author(s) and do not necessarily reflect the views of the National Science Foundation. Anthony P. Nicholson, Ramesh Pandey, and James Sites were funded in part by the U.S. Department of Energy's Office of Energy Efficiency and Renewable Energy (EERE) under the Solar Energy Technologies Office (SETO) Award No. DE-EE0008974. Amit H. Munshi received funding from the U.S. Department of Energy's EERE-SETO under Award No. DE-EE0008557. This work utilized the Summit supercomputer, which is supported by the National Science Foundation (awards ACI-1532235 and ACI-1532236), the University of Colorado Boulder, and Colorado State University. The Summit supercomputer is a joint effort of the University of Colorado Boulder and Colorado State University.

References

- (1) Klein, A.; Säuberlich, F.; Späth, B.; Schulmeyer, T.; Kraft, D. Non-Stoichiometry and Electronic Properties of Interfaces. *J. Mater. Sci.* **2007**, *42*, 1890–1900.
- (2) Margaritondo, G. Electronic Structure of Semiconductor Heterojunctions; Perspectives in Condensed Matter Physics; Springer Netherlands: Dordrecht, 1988; Vol. 1; p 4.
- (3) Klein, A. Energy Band Alignment at Interfaces of Semiconducting Oxides: A Review of Experimental Determination Using Photoelectron Spectroscopy and Comparison With Theoretical Predictions by the Electron Affinity Rule, Charge Neutrality Levels, and the Common Anion Rule. Thin Solid Films 2012, 520, 3721–3728.
- (4) Anderson, R. L. Experiments on Ge-GaAs Heterojunctions. Solid State Electron. 1962, 5, 341–351.
- (5) Mamiński, J.; Orlowski, B. Schottky Barrier Formation in CdTe Crystal. Surf. Sci. 1986, 168, 416–422.
- (6) Pugh, J. R.; Mao, D.; Zhang, J.-G.; Heben, M. J.; Nelson, A. J.; Frank, A. J. A Metal:p-n-CdTe Schottky-Barrier Solar Cell: Photoelectrochemical Generation of a Shallow p-Type Region in n-CdTe. J. Appl. Phys. 1993, 74, 2619–2625.
- (7) Demtsu, S.; Sites, J. Effect of Back-Contact Barrier on Thin-Film CdTe Solar Cells.

 Thin Solid Films 2006, 510, 320–324.
- (8) Koishiyev, G. T.; Sites, J. R.; Kulkarni, S. S.; Dhere, N. G. Determination of Back Contact Barrier Height in Cu(In,Ga)(Se,S)₂ and CdTe Solar Cells. 2008 33rd IEEE Photovoltaic Specialists Conference. 2008; pp 1–3.
- (9) Ali, A. M.; Rahman, K.; Ali, L. M.; Akhtaruzzaman, M.; Sopian, K.; Radiman, S.; Amin, N. A Computational Study on the Energy Bandgap Engineering in Performance Enhancement of CdTe Thin Film Solar Cells. Results Phys. 2017, 7, 1066–1072.

- (10) Song, T.; Moore, A.; Sites, J. R. Te Layer to Reduce the CdTe Back-Contact Barrier. IEEE J. Photovolt. 2018, 8, 293–298.
- (11) Munshi, A. H.; Kephart, J. M.; Abbas, A.; Shimpi, T. M.; Barth, K. L.; Walls, J. M.; Sampath, W. S. Polycrystalline CdTe Photovoltaics With Efficiency Over 18% Through Improved Absorber Passivation and Current Collection. Sol. Energy Mater. Sol. Cells 2018, 176, 9–18.
- (12) QuantumATK R-2020.09-SP1, Synopsys QuantumATK.
- (13) Nicholson, A. P.; Martinez, U.; Shah, A.; Thiyagarajan, A.; Sampath, W. S. Atomistic Modeling of Energy Band Alignment in CdTe(100) and CdTe(111) Surfaces. Appl. Surf. Sci. 2020, 528, 146832.
- (14) Nicholson, A. P.; Shah, A.; Thiyagarajan, A.; Sampath, W. S. Insights Toward Chlorine Passivation Effects on Electronic Structures of CdTe(100) and CdTe(111) Surfaces via Atomistic Modeling. Surf. Interfaces 2021, 27, 101458.
- (15) Romeo, A. In *McEvoy's Handbook of Photovoltaics*, 3rd ed.; Kalogirou, S. A., Ed.; Academic Press, 2018; Chapter I-3-B, pp 309–369.
- (16) Anzin, V. B.; Eremets, M. I.; Kosichkin, Y. V.; Nadezhdinskii, A. I.; Shirokov, A. M. Measurement of the Energy Gap in Tellurium Under Pressure. *Phys. Status Solidi A* 1977, 42, 385–390.
- (17) Nicholson, A. Density Functional Theory and Green's Function Approach to Investigate Cadmium Telluride Based Thin Film Photovoltaics. Ph.D. thesis, Colorado State University, 2020.
- (18) Stradi, D.; Jelver, L.; Smidstrup, S.; Stokbro, K. Method for Determining Optimal Supercell Representation of Interfaces. *J. Phys. Condens. Matter* **2017**, *29*, 185901.
- (19) Marple, D. T. F. Effective Electron Mass in CdTe. Phys. Rev. 1963, 129, 2466–2470.

- (20) Lutz, M.; Stolze, H.; Grosse, P. The Masses of Free Holes and Electrons in Tellurium. *Phys. Status Solidi B* **1974**, *62*, 665–675.
- (21) Long, F.; Hagston, W. E.; Harrison, P.; Stirner, T. The Structural Dependence of the Effective Mass and Luttinger Parameters in Semiconductor Quantum Wells. J. Appl. Phys. 1997, 82, 3414–3421.
- (22) Rubio-Ponce, A.; Olguín, D.; Hernández-Calderón, I. Calculation of the Effective Masses of II-VI Semiconductor Compounds. *Superficies y Vacío* **2003**, *16*, 26–28.
- (23) Lalitha, S.; Karazhanov, S.; Ravindran, P.; Senthilarasu, S.; Sathyamoorthy, R.; Janabergenov, J. Electronic Structure, Structural and Optical Properties of Thermally Evaporated CdTe Thin Films. *Physica B Condens. Matter* **2007**, *387*, 227–238.
- (24) Peng, H.; Kioussis, N.; Snyder, G. J. Elemental Tellurium as a Chiral *p*-Type Thermoelectric Material. *Phys. Rev. B* **2014**, *89*, 195206.
- (25) Burgelman, M.; Nollet, P.; Degrave, S. Modelling Polycrystalline Semiconductor Solar Cells. *Thin Solid Films* **2000**, *361-362*, 527–532.
- (26) Pandey, R.; Shimpi, T.; Munshi, A.; Sites, J. R. Impact of Carrier Concentration and Carrier Lifetime on MgZnO/CdSeTe/CdTe Solar Cells. *IEEE J. Photovolt.* 2020, 10, 1918–1925.
- (27) He, X.; Wu, L.; Hao, X.; Zhang, J.; Li, C.; Wang, W.; Feng, L.; Du, Z. The Band Structures of Zn_{1-x}Mg_xO(In) and the Simulation of CdTe Solar Cells With a Zn_{1-x}Mg_xO(In) Window Layer by SCAPS. *Energies* **2019**, *12*, 291.
- (28) Teyou Ngoupo, A.; Ouédraogo, S.; Zougmoré, F.; Ndjaka, J. M. B. New Architecture Towards Ultrathin CdTe Solar Cells for High Conversion Efficiency. *Int. J. Photoenergy* 2015, 2015, 1–9.

- (29) Matin, M. A.; Tomal, M. U.; Robin, A. M.; Amin, N. Numerical Analysis of Novel Back Surface Field for High Efficiency Ultrathin CdTe Solar Cells. *Int. J. Photoenergy* **2013**, *2013*, 1–8.
- (30) Kanevce, A.; Reese, M. O.; Barnes, T. M.; Jensen, S. A.; Metzger, W. K. The Roles of Carrier Concentration and Interface, Bulk, and Grain-Boundary Recombination for 25% Efficient CdTe Solar Cells. J. Appl. Phys. 2017, 121, 214506.
- (31) Guo, J.; Mannodi-Kanakkithodi, A.; Sen, F. G.; Schwenker, E.; Barnard, E. S.; Munshi, A.; Sampath, W.; Chan, M. K. Y.; Klie, R. F. Effect of Selenium and Chlorine Co-Passivation in Polycrystalline CdSeTe Devices. Appl. Phys. Lett. 2019, 115, 153901.
- (32) Olender, K.; Wosiński, T.; Mąkosa, A.; Dłużewski, P.; Kolkovsky, V.; Karczewski, G. Native Deep-Level Defects in MBE-Grown p-Type CdTe. Acta Physica Polonica A 2011, 120, 946–949.
- (33) Ablekim, T.; Swain, S. K.; McCoy, J.; Lynn, K. G. Defects in Undoped p-Type CdTe Single Crystals. *IEEE J. Photovolt.* **2016**, *6*, 1663–1667.
- (34) McCandless, B.; Buchanan, W.; Sriramagiri, G.; Thompson, C.; Duenow, J.; Albin, D.; Jensen, S. A.; Moseley, J.; Al-Jassim, M.; Metzger, W. K. Enhanced p-Type Doping in Polycrystalline CdTe Films: Deposition and Activation. *IEEE J. Photovolt.* 2019, 9, 912–917.
- (35) Capers, M.; White, M. The Electrical Properties of Vacuum Deposited Tellurium Films.

 Thin Solid Films 1973, 15, 5–14.
- (36) Steiner, K.; Chen, W.; Pasquarello, A. Band Offsets of Lattice-Matched Semiconductor Heterojunctions Through Hybrid Functionals and G_0W_0 . Phys. Rev. B **2014**, 89, 205309.

- (37) Weston, L.; Tailor, H.; Krishnaswamy, K.; Bjaalie, L.; Van de Walle, C. Accurate and Efficient Band-Offset Calculations From Density Functional Theory. *Comput. Mater. Sci.* **2018**, *151*, 174–180.
- (38) Scheer, R.; Schock, H.-W. Chalcogenide Photovoltaics: Physics, Technologies, and Thin Film Devices; Wiley-VCH Verlag GmbH & Co. KGaA: Weinheim, 2011; p 178.
- (39) Rigaux, C. Etude de la Structure de Bandes du Tellure par les Phenomenes de Transport. J. Phys. Chem. Solids 1962, 23, 805–817.
- (40) Van de Walle, C. G. Band Lineups and Deformation Potentials in the Model-Solid Theory. *Phys. Rev. B* **1989**, *39*, 1871–1883.
- (41) Franciosi, A.; Van de Walle, C. G. Heterojunction Band Offset Engineering. Surf. Sci. Rep. 1996, 25, 1–140.
- (42) Butler, K. T.; Sai Gautam, G.; Canepa, P. Designing Interfaces in Energy Materials Applications With First-Principles Calculations. NPJ Comput. Mater. 2019, 5, 19.
- (43) Fritsche, J.; Kraft, D.; Thißen, A.; Mayer, T.; Klein, A.; Jaegermann, W. Band Energy Diagram of CdTe Thin Film Solar Cells. *Thin Solid Films* **2002**, 403-404, 252-257, Proceedings of Symposium P on Thin Film Materials for Photovoltaics.
- (44) Kraft, D.; Thissen, A.; Broetz, J.; Flege, S.; Campo, M.; Klein, A.; Jaegermann, W. Characterization of Tellurium Layers for Back Contact Formation on Close to Technology Treated CdTe Surfaces. J. Appl. Phys. 2003, 94, 3589–3598.
- (45) Fritsche, J.; Klein, A.; Jaegermann, W. Thin Film Solar Cells: Materials Science at Interfaces. Adv. Eng. Mater. 2005, 7, 914–920.
- (46) Odkhuu, D.; Miao, M.-S.; Aqariden, F.; Grein, C.; Kioussis, N. Atomic and Electronic Structure of CdTe/Metal (Cu, Al, Pt) Interfaces and Their Influence to the Schottky Barrier. J. Appl. Phys. 2016, 120, 185703.

- (47) Shah, A.; Munshi, A. H.; Nicholson, A. P.; Thiyagarajan, A.; Pozzoni, U. M.; Sampath, W. S. Atomistic Modeling of Energy Band Alignment in CdSeTe Surfaces. Appl. Surf. Sci. 2021, 544, 148762.
- (48) Smidstrup, S.; Stradi, D.; Wellendorff, J.; Khomyakov, P. A.; Vej-Hansen, U. G.; Lee, M.-E.; Ghosh, T.; Jónsson, E.; Jónsson, H.; Stokbro, K. First-Principles Green's-Function Method for Surface Calculations: A Pseudopotential Localized Basis Set Approach. Phys. Rev. B 2017, 96, 195309.
- (49) Niles, D. W.; Li, X.; Sheldon, P.; Höchst, H. A Photoemission Determination of the Band Diagram of the Te/CdTe Interface. J. Appl. Phys. 1995, 77, 4489–4493.
- (50) Jiao, Y.; Hellman, A.; Fang, Y.; Gao, S.; Käll, M. Schottky Barrier Formation and Band Bending Revealed by First-Principles Calculations. *Sci. Rep.* **2015**, *5*, 11374.
- (51) Kandilarov, B.; Detcheva, V.; Primatarowa, M. Energy-Band Profile and Interface Potential Step in the Theory of Semiconductor Heterojunctions. Surf. Sci. 1980, 99, 174–182.
- (52) Niles, D. W.; Li, X.; Albin, D.; Rose, D.; Gessert, T.; Sheldon, P. Evaporated Te on CdTe: A Vacuum-Compatible Approach to Making Back Contact to CdTe Solar Cell Devices. Prog. Photovolt. 1996, 4, 225–229.
- (53) Li, J.; Kioussis, N.; Aqariden, F.; Grein, C. Thermodynamic and Stoichiometric Stability of the Cd-Terminated CdTe (111) Surface. *Phys. Rev. B* **2012**, *85*, 235306.
- (54) Kowalski, B.; Orłowski, B.; Ghijsen, J. Oxide Formation on the CdTe(111)A (1×1) Surface. Appl. Surf. Sci. 2000, 166, 237–241.

Graphical TOC Entry

